Research Article

Dynamic Response of the Steel Plate Under the Impact of High-Speed Coal Projectile

Chuanjie Zhu [ID], Qi Yu, Ximiao Lu, Baiquan Lin [ID], and Cong Ma

Faculty of Safety Engineering, China University of Mining and Technology, Xuzhou 221116, China

Correspondence should be addressed to Chuanjie Zhu; anq021@126.com

The coal-rock projectiles induced by gas explosions in coal mines have a strong destructive effect on mine facilities and equipment, which are mostly made of steel. The LS-DYNA is used to simulate the process of coal projectile striking the steel plate. The results show that during the failure process, the morphological change of the projectile consists of three stages including plastic deformation, partial crushing, and complete crushing, and the steel plate pits at the impact point. The duration of the stress peak value of the steel plate increases as the impact velocity increases. The farther away from the center point, the smaller the stress peak value is, and the shorter the duration is. When the impact velocity is 100 m/s and 300 m/s, the axial velocity curve at the impact point of the projectile is pulsating. When the impact velocity reaches 500 m/s, the axial velocity of the projectile rapidly increases and then tends to be stable. As the impact velocity increases, the energy absorbed by the steel plate increases, and the rate of increase also increases. However, the proportion between the absorbed energy of the steel plate and the initial kinetic energy of the projectile decreases. The projectile conversion energy of the 1 mm steel plate is slightly larger than that of 1.5 mm and 2 mm steel plates, and the energy absorbed by the steel plate decreases with the increase in thickness of the steel plate. When the thickness of the steel plate is more than 2 mm, the thickness of the steel plate has little effect. The results of the study have a direct sense for the antiknock design of coal mine facilities and equipment.

1. Introduction

Gas explosion is the most serious disaster in the process of coal mine production caused by mass casualties; gas explosion has become a bottleneck to restrict the safety production of coal. Once the gas explosion occurs in a coal mine, the formation of high-temperature and high-pressure shock waves will cause impact damage to materials; on the other hand, it will also induce secondary disasters. For example, high-speed blocks of rock sucked by shock waves will also cause secondary impact damage to materials; meanwhile, the broken rock will also reflect on the surrounding equipment or personnel to cause further damage, which not only poses a great threat to people's life safety but also causes great damage to various mining equipment and roadways under the mine, resulting in significant losses.

A large number of research studies on gas explosion mechanism and the propagation characteristics of explosion shock waves through experiments, theoretical derivation, and numerical simulation have been conducted by domestic and foreign scholars to effectively prevent and control gas explosive accidents, and researchers derived the general damage and injury guidelines of explosion shock waves [1–7]. According to a large quantity of gas explosion disaster accident site data, the impact airflow immediately behind the shock wave front will also produce fatal injury and destructive effects on people or other equipment with violent impact, the consequences of which cannot be ignored [8–10]. Therefore, Yang et al. [11] derived the model of the decay of the blast shock airflow velocity based on theoretical derivation and experimental verification. It concluded that the shock airflow velocity can easily reach 100 m/s while the velocity can reach 1000 m/s near the explosion source. Lang

et al. [12] analyzed the destructive nature of gas explosion through experiments and reported that the calculated velocity of debris entrained by impact airflow will be smaller than the actual value.

This paper focuses on the problem that the spherical coal-rock projectile is impinging on the armor steel plate protective structure. Experimental research and numerical simulation are mainly used as quantitative research methods for the hypervelocity impact problem of the thin plate. The physical processes and broken phenomena of hypervelocity impact of spherical projectiles on thin plates have been concerned by researchers. Scholars at home and abroad have made a lot of research results on the distribution of debris clouds generated by the impact. Piekutowski [13] conducted a study on the hypervelocity collision problem with different materials, projectile shapes, impact inclinations, impact speeds, and the ratio of projectile diameter to target thickness through experimental methods. According to the pictures of the debris cloud and the changes of internal structure, the results showed that the destructive ability increased as the size of fragments increased, and the destructive ability of the disk-shaped projectile and the cylindrical projectile was obviously stronger than that of the spherical projectile. Bashurov et al. [14] studied on the ultrahigh-speed positive collision of steel balls and the 45° oblique collision with a steel or aluminum alloy single-layer target plate. It concluded that the number of collision fragments increased significantly as the impact speed increased, while the size of fragments decreased obviously. Maiden and Mcmillan [15] qualitatively described the crushing process of a hypervelocity projectile hitting a thin plate and considered that the crushing of target material is caused by the net tensile stress at a certain position of the material exceeding the dynamic breaking strength of the material caused by the sparse wave. Iyer et al. [16] studied the impact of a 2017-T4 aluminum ball with a diameter of 2.35 mm on the Ti-6Al-4V shield at a speed of 7 km/s. The results showed that the damage modes at the bottom of the crater included microcracks, shear bands, large grain deformation, and recrystallization.

At present, compared with research studies on the attenuation characteristics of explosive blast velocity, there are relatively few studies on the impact and destruction process of coal-rock fragments entrained by the airflow on the object at home and abroad. Dahl and Schultz [17] studied the propagation characteristics of stress waves in the process of hypervelocity impact through LS-DYNA simulation software. It considered that the collision materials broke because the tensile stress at a point in the sparse wave material exceeded the breaking tenacity of materials. Based on the smooth particle algorithm of LS-DYNA software, Guan et al. [18] analyzed the fragmentation behaviors of aluminum ball projectiles impacting an aluminum mesh protective screen at high velocity and debris cloud characteristics of projectile. Yang [19] investigated the deformation field caused by a rigid projectile impacting 316L stainless steel and derived the distribution of residual stress in the crater by experiments with LS-DYNA numerical simulations.

The impact damage process of debris entrained by gas explosion impact airflow on underground equipment differs from other elastic material projectiles, which produces damage to facilities or equipment but also breaks to form secondary reflection debris for further formation of destruction. Normally, complex engineering problems can be solved by discrete numerical methods. The finite element method of LS-DYNA software based on traditional continuum mechanics provides a good teaching method for the study of steel penetration problems. It is difficult to observe the crater formation of the target plate through experiments, but the crater formation process of the target plate can be fully understood with the help of numerical simulation. Numerical simulation can qualitatively simulate the transient phenomenon of the projectile-steel plate interaction and give the numerical solution of the entire interaction process, which makes people have a clear and specific perceptual understanding of the armor-piercing process [20, 21]. There are few researches on the above process; in this study, the damage effects formed by coal-rock projectiles hitting steel plates of different thickness with different velocities in a forward direction were revealed based on the LS-DYNA numerical simulation method. Moreover, the stress distribution characteristics and deformation of steel plates and coal-rock projectiles, the rebounded or crushed scattering process, and speed characteristics were analyzed.

2. Numerical Simulation

2.1. FEM Model. Under the same conditions, the spherical projectile has the least destructive ability, while the damage degree of nonspherical projectile is related to the slenderness ratio and less likely the projectile is to break when the slenderness ratio is greater than 1 [22]. Therefore, in this paper, a long rod type of projectile with a diameter of 4 mm and a rod length of 2 mm is used as the coal-rock experimental material to study the impact process of coal-rock projectiles and the characteristics of the fragment cloud when the projectile rebounds. The length and width of the steel plate are 24 cm × 24 cm; the thickness is 1 mm, 1.5 mm, and 2 mm; and the impact velocities of the projectiles are 100 m/s, 300 m/s, 500 m/s, 800 m/s, and 1000 m/s, respectively. According to the symmetry of the structure, the 1/4 model was established allowing for calculated time and period, and the finite element geometry model is shown in Figure 1(a). The whole process of the simulation adopted Lagrange algorithm, finite element, and face-to-face eroding contact. Considering the accuracy and time-consumption of the calculation, the mesh was densely divided in the 2 cm × 2 cm square area around the collision point of the steel plate, and the mesh is sparsely divided in other areas. The specific mesh generation is shown in Figure 1(b). Generally speaking, different impact conditions such as impact material, shape, size, impact angle, and velocity can all lead to large differences in the debris cloud generated by high-speed impact phenomena [23]. Usually, a model is only suitable for describing the debris cloud generated within a certain range of impact conditions. On the whole, it is generally inaccurate to assume that the pressure peak on the
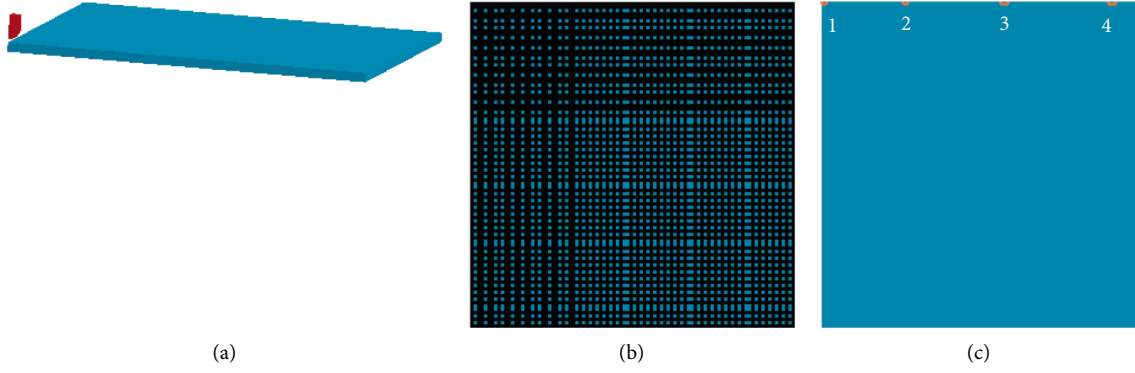
(a)   (b)   (c)

FIGURE 1: Figure of the numerical simulation process diagram. (a) Figure of finite element model; (b) figure of grid partition; (c) figure of observation point position.

TABLE 1: Material parameters of coal.

Materials	Density (g·cm^{-3})	Shear modulus (GPa)	Poisson	Friction angle (°)	Cohesion (Pa)	Divergence angle (°)
Coal	1.4	0.8	0.3	0.55	5×10^4	1.6

axis decreases linearly with distance. Therefore, in this paper, the four observation points of the material model are set on the same side to observe the change and development law of the radial stress of the contact wave front when the projectile penetrates the steel plate face to face. In addition, there were four observation points set to investigate the damage effect of high-speed coal-rock projectiles impacting on the steel plate, of which measurement point 1 was the geometric center point of the steel plate, and the distances between measurement points 2, 3, and 4 from the center point (measurement point 1) are 18 mm, 36 mm, and 54 mm, respectively, as shown in Figure 1(c).

2.2. Material Models. In this paper, coal is selected as the projectile material, and its material model is selected as the Drucke–-Prager model from the LS-DYNA material library, which obeys the D-P criterion. The main parameters are shown in Table 1.

The steel plate is made of armor steel, and its material model adopts the linear isotropic strain hardening material model (Johnson–Cook), following the von Mises criterion, and the equation can be expressed as follows:

$$\sigma_e = \left[A + B(\varepsilon_e^p)^N \right] (1 + C \ln \dot{\varepsilon}^*) \left[1 - (T^*)^M \right], \quad (1)$$

where ε_e^p is the equivalent plastic strain, $\dot{\varepsilon}^*$ the relative equivalent plastic strain rate, A the yield stress; B the strain hardening, N the strain hardening exponent, C the strain rate correlation factor, M the temperature dependent factor, and T^* the relative temperature in K; and the equation can be expressed as follows:

$$T^* = \frac{T - T_R}{T_M - T_R}, \quad T_R \le T \le T_M, \quad (2)$$

where T is the outdoor temperature, T_R the indoor temperature, and T_M the dissolving temperature.

The fracture of the Johnson–Cook material model is derived by the following cumulative damage criterion:

$$D = \sum \left(\frac{\Delta \varepsilon_e^p}{\varepsilon_f^p} \right), \quad (3)$$

where ε_e^p is the plastic strain increment for one integration cycle, and ε_f^p is the effective fracture strain at the current time step. The cumulative damage criterion refers that when the damage parameter D exceeds 1, the material fails.

The expression of the fracture model is defined by the Johnson–Cook material model as follows:

$$\varepsilon_f^p = \left[D_1 + D_2 \exp \left(D_3 \frac{\sigma_m}{\sigma_g} \right) \right] (1 + D_4 \ln \dot{\varepsilon}^*) (1 + D_5 T^*), \quad (4)$$

where D_1, D_2, D_3, D_4, and D_5 are constants related to materials; σ_m is the equivalent stress. $D_1 \sim D_3$ can be obtained by performing different stress triaxiality experiments at the reference strain rate and reference temperature. The strain rate influence constant D_4 can be obtained by the tensile test at different strain rates at the reference temperature. The temperature influence constant D_5 can be obtained by the tensile test at different temperatures at the reference strain rate. The specific material parameters are shown in Table 2.

Since the experiment of strain rate and temperature effect on failure strain has not been carried out, and considering that the stress triaxiality has the most significant effect on the failure of metal materials, this paper focuses on the fitting of parameters D_1–D_3 on the basis of D_4 and D_5 parameters being zero. The material parameters of the steel plate in this paper are mainly derived from the work of Bao et al. [24], and Chen et al. [25]. The relationship between the failure strain and the stress triaxiality can be obtained according to the quasi-static cylindrical compression experiment, the round rod torsion test, the uniaxial tensile test,

TABLE 2: Material parameters of steel plate.

Elasticity modulus (GPa)	Young's modulus (N·m^{-1})	Poisson	Density (g·cm^{-3})	A (N·m^{-1})	B (N·m^{-1})	N	C	M	$\dot{\varepsilon}^*$ (μ·s^{-1})	T_M (K)	T_R (K)	Specific heat C_p	Stress limit P_C (N/m)	D_1	$D_2 \sim D_5$
71.4	2.1×10^{12}	0.22	7.83	0.122	5.1×10^{-2}	0.26	0.014	1.03	10^{-6}	1793	294	0.477×10^{-5}	-9	2.5	0

TABLE 3: Experimental parameters of projectile material.

Material	Shape	Diameter (mm)	Quality (g)	Impact speed	Density
Volcanic rock	Sphericity	6.92	0.20	1.30 km/s ~ 2.80 km/s	1.22 g·cm^{-3}

TABLE 4: Parameters of steel plate calculation model.

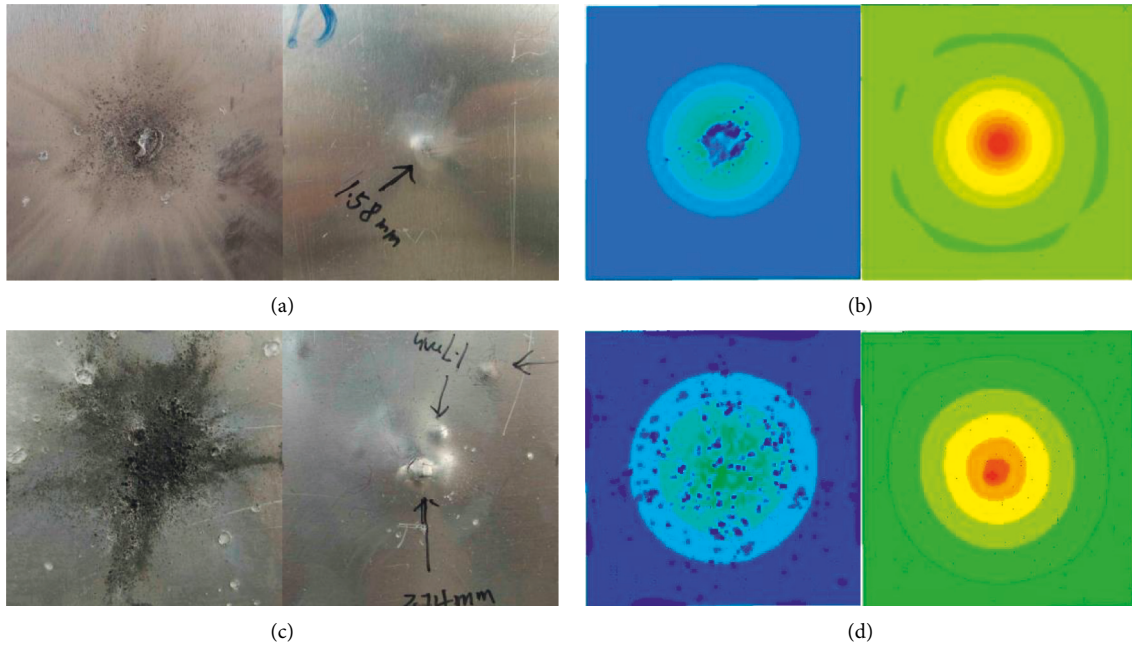| Material	Size	Front target (mm)	Rear target (mm)	Target spacing (mm)
Aluminum alloy	20 cm × 20 cm	1	3	100

(a)

(b)

(c)

(d)

FIGURE 2: Comparison of high-speed impact test and simulation results of two different impact velocities. (a) High-speed impact test results at 1.44 km/s; (b) high-speed impact simulation results at 1.44 km/s; (c) high-speed impact test results at 2.78 km/s; (d) high-speed impact simulation results at 2.78 km/s.

and the notched tensile test. Combining the relationship between different initial stress triaxiality and failure strain obtained by numerical simulation and experimental results, it can be seen that the change of failure strain under different stress triaxiality is basically the same. After decoupling equation (4), the parameters in the first term are fitted, and finally the parameters $D_1 = 2.5$, $D_2 = 0$, and $D_3 = 0$ in the J-C failure model are obtained approximately.

2.3. Validation of Numerical Simulation. In this study, a set of experimental conditions of rock projectiles impacting the Whipple protective structure was taken to verify the validity of the numerical simulation method as an example of Harbin

Institute of Technology, with projectile diameters ranging from 6.30 mm to 7.40 mm, projectile masses ranging from 0.15 g to 0.30 g, and impacting velocities ranging from 1.30 km/s to 2.80 km/s. The experimental parameters of rock projectiles and steel plates are shown in Tables 3 and 4. The comparison of the calculated results with the experimental results is shown in Figure 2. As can be seen from the figure, the numerical simulations and experimental observations are in general agreement. The bulge height of the rear plate at the impact velocity of 1.42 km/s was selected to further verify the accuracy of the results. It has been shown that the experimental bulge height is 1.58 mm while the numerical simulation bulge height is 1.68 mm, and the error between the experiment and simulation is 6.3%, which indicates that
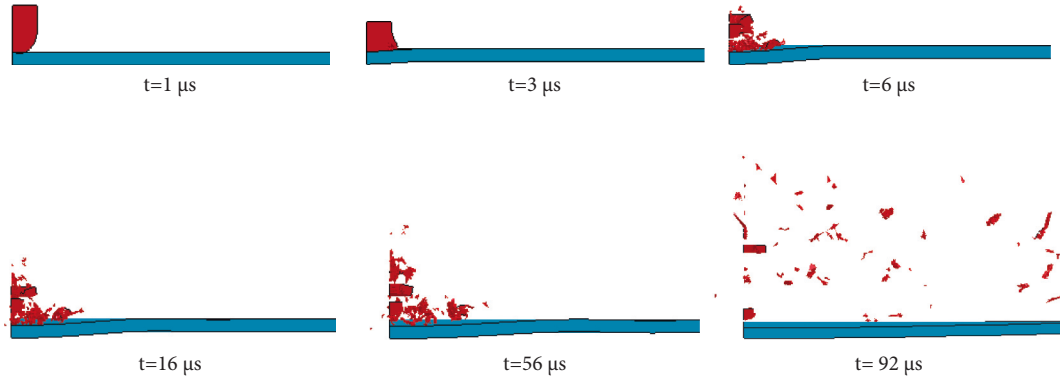
FIGURE 3: Impact failure process of projectile.

the simulation results and experimental results are basically in agreement [26]. In summary, the simulation results are in good agreement with the experimental results, fully verifying the effectiveness of the numerical simulation method. Based on this, the characteristic of steel plate stricken by coal-rock projectiles under high-velocity is further analyzed.

3. Numerical Modeling Results and Analysis

3.1. Impact Fracture Behavior. In this paper, the coal rock is selected as the material hitting a steel plate with a thickness of 1 mm at a speed of 500 m/s, to analyze the process of projectile impacting the steel plate, and the damage process of projectile impact is shown in Figure 3. According to the figure, when the impact time $t = 1\,\mu s$, neither the steel plate nor the projectile changes significantly due to the initial contact; when $t = 3\,\mu s$, the head of the projectile begins to plastically deform, and the steel plate also shows a slight concave tendency; when $t = 6\,\mu s$, the projectile starts to break from the head and then spreads to the periphery to move backward as a whole, while the steel plate begins to deform and sag downward; when $t = 16\,\mu s$, the projectile is basically broken into larger fragments and the steel plate forms pits. At this time, the bulge height of the steel plate reaches the maximum value of 0.52 mm, as shown in Figure 4. When $t = 56\,\mu s$, the projectile is more completely broken into smaller and numerous fragments and the steel plate begins to recover from deformation; in the range of $t = 16 \sim 56\,\mu s$, the shock wave in the steel plate propagates around and its deformation remains basically invariable; after $56\,\mu s$, the bulge height of the steel plate continues to spread in the form of waves; when $t = 92\,\mu s$, the projectile is completely broken, in which the size of fragments becomes smaller and the number of fragments increases, and the steel plate recovers partial deformation.

The morphological changes of coal-rock projectiles during the entire failure process basically include three stages which are plastic deformation, partial crushing, and complete crushing.

(a) When $t = 0 \sim 16\,\mu s$, the projectile just touches the steel plate within $1 \sim 3\,\mu s$ during the initial impact process. When the steel plate is subjected to local impact load, all projectiles are not broken due to the
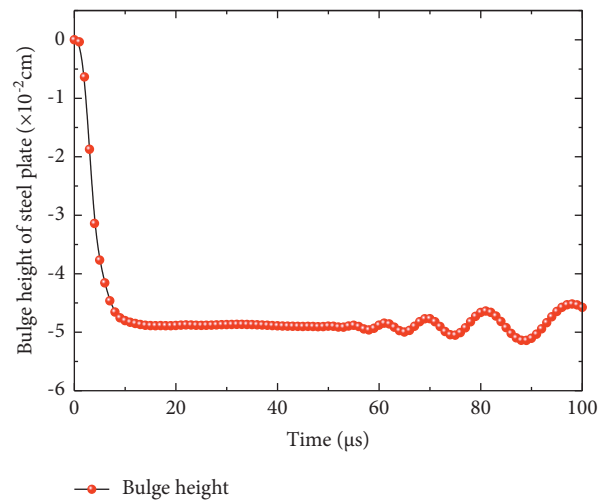

FIGURE 4: Deformation depth of steel plate.

low impact speed, only producing different degrees of plastic deformation. With the increase of the impact speed, the plastic deformation is more significant, and the deformation of the front surface is larger than that of the rear surface. After $t = 5\,\mu s$, as the impact velocity of the projectile continues to act, the plastic deformation of the projectile increases and changes more obviously with the increase of the thickness of steel plate. With the increase of the impact velocity, the front surface gradually deforms to approximate a plane in which the axial dimension further decreases and the radial dimension further increases. The rear surface appears spalling, which occurs over time. The projectile peels off to form an approximately hemispherical shell-like debris cloud that expands with the overall movement of the debris cloud. When t reaches between $10\,\mu s$ and $16\,\mu s$, the projectile body at different impact speeds has been basically broken. At this time, the steel plate forms a pit with larger size fragments in which the height of the steel plate bulge reaches the maximum value.

(b) When $t = 16 \sim 56\,\mu s$, as the initial impact velocity continues to increase, the size of the fragments
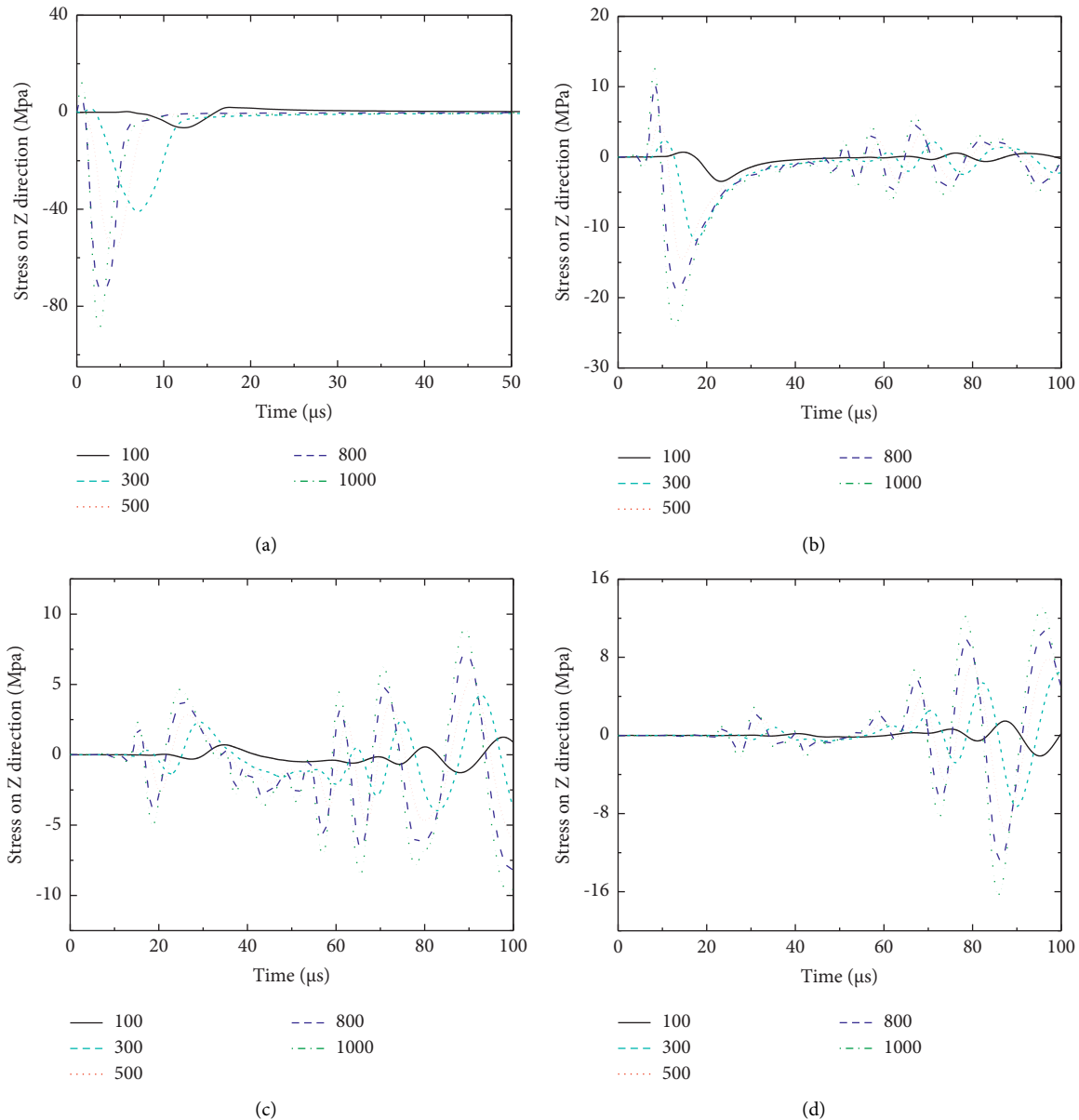
FIGURE 5: The stress curve of steel plate at different impact velocity. (a) Point 1; (b) Point 2; (c) Point 3; (d) Point 4.

formed by the exfoliation of the surface material after the projectile gets further decreased. The main material of the projectile was completely broken to form a fragment cloud and expanded radially, which indicates that the shock wave intensity increased enough to completely break the entire projectile. The shock wave in the steel plate propagates around, and the deformation of the steel plate remains basically unchanged at this time which means that the height of the bulge remains basically unchanged.

(c) After t is 56 μs, the bulge height of the steel plate continuously propagates in the form of waves. When the impact time approaches 100 μs, the projectile and the steel plate have been separated with the end of the impact process. The steel plate generates deformation energy, and its stress continuously propagates in

a similar sinusoidal curve. With the increase of the impact speed, the fluctuation of the curve is more obvious and the peak value of the steel plate stress is larger.

In short, the steel plate changes from no obvious deformation to obvious deformation, forming pits at the impact point, and finally has recovered partial deformation. Due to the propagation of the stress wave inside the projectile during the impact process, the morphology of the projectile and the steel plate changes with the intensity of the stress wave and the position of the interaction at different times.

3.2. Impact of Projectile Velocity on the Damage Effect. In this paper, the Z-direction stress and strain at the center point of the 1.5 mm steel plate and three measurement points with
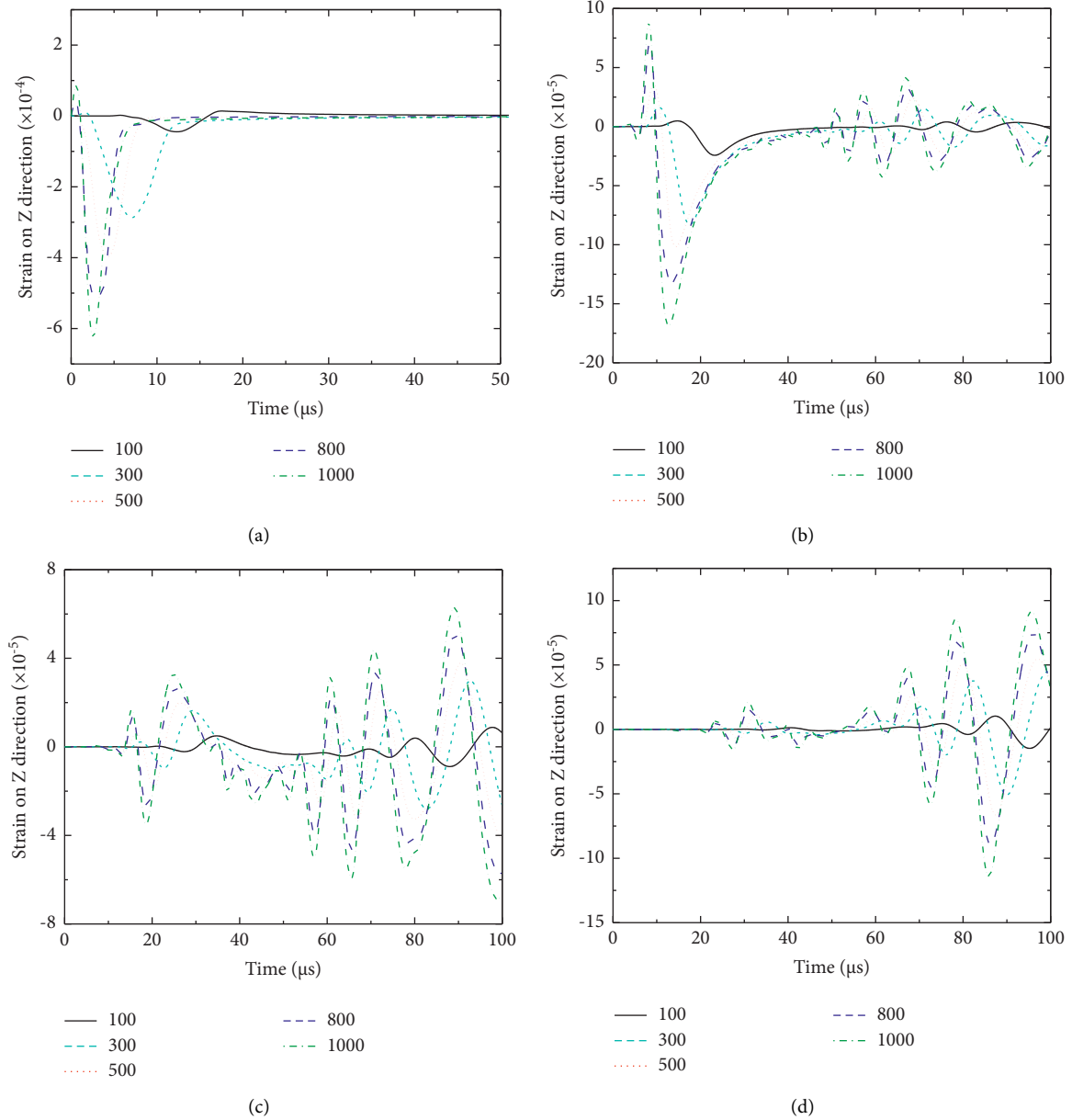
(a)

(b)

(c)

(d)

FIGURE 6: The strain curve of steel plate at different impact velocity. (a) Point 1; (b) Point 2; (c) Point 3; (d) Point 4.

equal spacing of 18 mm are selected to analyze the impact of the projectile velocity on the damage effect of the steel plate. As shown in Figures 5 and 6, the change trend of the stress curve is basically identical to the strain curve.

After the coal-rock projectile hits the steel plate with a thickness of 1.5 mm, the disturbance of the particles of each part of the object by the suddenly applied load cannot occur concurrently due to the inertia of the material, which undergoes a propagation process gradually spreading from the locally disturbed zones to the undisturbed zones [27–29]. It can be concluded from Figure 5 that the stress of the steel plate varies with the impact velocity. As shown in Figure 5(a), at the center point (point 1), when the impact velocity of the coal-rock projectile is $v = 100$ m/s, the pressure on the steel plate increases during the impact process

which gradually recovers to deform with the stress that is decreasing and finally tending to zero due to the plastic deformation; when the velocity reaches 500 m/s, the steel plate undergoes the tensile stress because the projectile has been broken at this moment. As shown in Figures 5(b)–5(d), at 18 mm, 36 mm, and 54 mm from the center point (point 2, point 3, point 4), when the impact time $t < 30\,\mu$s, the change in trend of the stress curve of the steel plate is basically identical to that at point 1 when $v \geq 500$ m/s; the projectile gets separated from the steel plate where the deformation energy is produced when $t > 50\,\mu$s, and the stress of the steel plate continues to propagate in a similar sinusoidal curve, where the more obvious the curve fluctuations are as the impact velocity increases, the larger the peak value of the steel plate stress is.
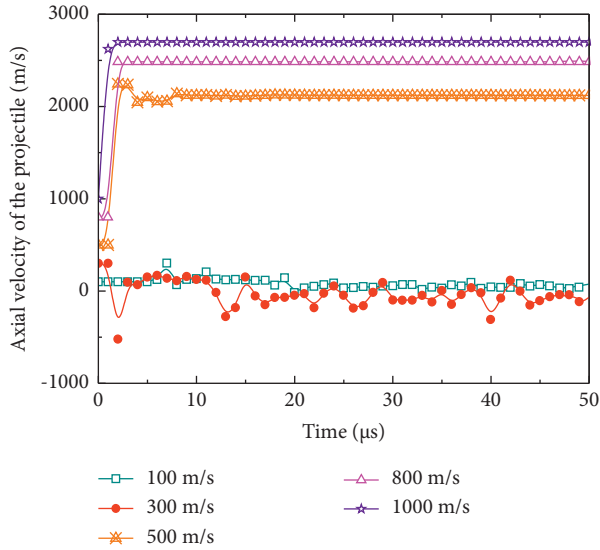
FIGURE 7: Figure of projectile impact point's axial velocity under different impact velocity.

FIGURE 8: Figure of energy change under different impact velocity.

It can be concluded by comparing Figures 5(a)~ 5(d) that the duration of the peak stress on the steel plate is affected by the speed and the distance from the center point. When the impact time $t < 30 \mu$s, the duration of the peak stress increases as the impact velocity increases and the peak value decreases as the distance from the center point increases. The peak stress increases as the distance from the center point increases when $t > 30 \mu$s, changing more significantly especially after 50μs.

Figure 7 shows the changing curve of the axial velocity at the impact point of the coal-rock projectiles which hit the 1.5 mm steel plate with a speed of 100 m/s, 300 m/s, 500 m/s, 800 m/s, and 1000 m/s. As shown in Figure 7, when the impact velocity is 100 m/s and 300 m/s, the axial velocity at the impact point of the projectile varies in pulsation because the bullet attached to the impact point of the projectile produces elastic deformation after the end of the impact process [30], while the axial velocity of 300 m/s fluctuates more indeed because the deformation generated during 300 m/s impacts greater than 100 m/s impact. When the impact velocity reaches more than 500 m/s, the axial velocity of the projectile increases sharply and then gradually stabilizes; the projectile spreads around in the form of fragments, and the impact point acquires a certain velocity, causing harm easily with the velocity of the fragments exceeding the initial velocity [31].

When the projectile hits the steel plate at high speed, most of its initial kinetic energy continues to be converted into the kinetic energy of the projectile fragments. Meanwhile, the rest of the initial kinetic energy will be used for plastic deformation of the impact body, dynamic crushing, and conversion into internal energy which increases the temperature of local materials [32, 33]. The energy absorbed by the steel plate is not only affected by the impact conditions such as the initial velocity of the projectile, the thickness of the steel plate, and the diameter of the projectile but also is related to the material parameters of the projectile
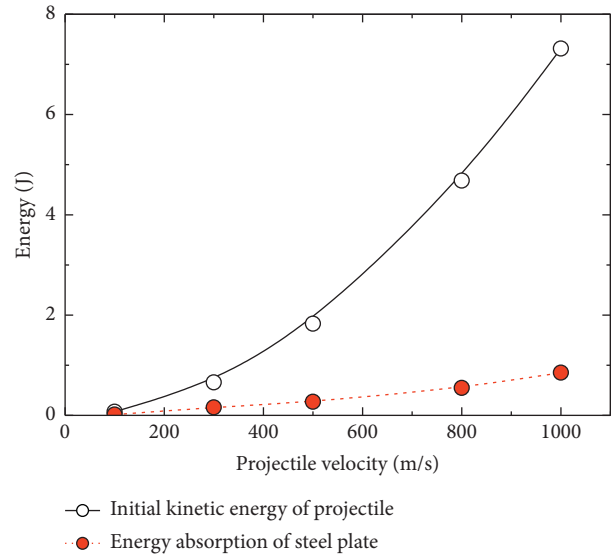
and the steel plate. It is considered that the normalized energy dissipated and absorbed is greatly affected by the strength of the steel plate and the quality of the projectile.

Figure 8 shows the change of energy during the impact process. The energy absorbed by the steel plate and the rate of energy growth both increase as the impact velocity increases, while the ratio of the energy absorbed by the steel plate to the initial kinetic energy of the projectile decreases accordingly. It can be concluded that most of the kinetic energy of the projectile during the high-speed impact has been consumed in the form of deformation energy of the target plate material [34], and the deformation of the steel plate increases, the more easily the projectile is broken and the more complete the fragmentation is, which results in the increase of the energy consumed by fragments throwing and the decrease of the residual energy of the steel plate.

3.3. Impact of Steel Plate Thickness on the Damage Effect. The shock wave generated in the steel plate transfers a part of the kinetic energy of the projectile to the steel plate, which increases the internal energy of the steel plate under compression. When the reflected rarefaction wave is generated, the part of the compressed material begins to undergo an isentropic process of unloading, which increases the momentum of the material and expands with forward movements. Considering the combined action of various factors such as shock wave and tensile wave, the fragments produced by the impactor material expanded into shells and ejected to the plate [35, 36].

The maximum fragment size decreases as the thickness of the steel plate increases under the condition of constant impact velocity. When the thickness of the steel plate is 1.50 mm and 2.00 mm, the size of the fragments differentiates little, which reflects that the fragmentation degree of the main part of the projectile increases first and then does not change with the increase of the thickness of the steel plate. The impact strength of the main part of the projectile
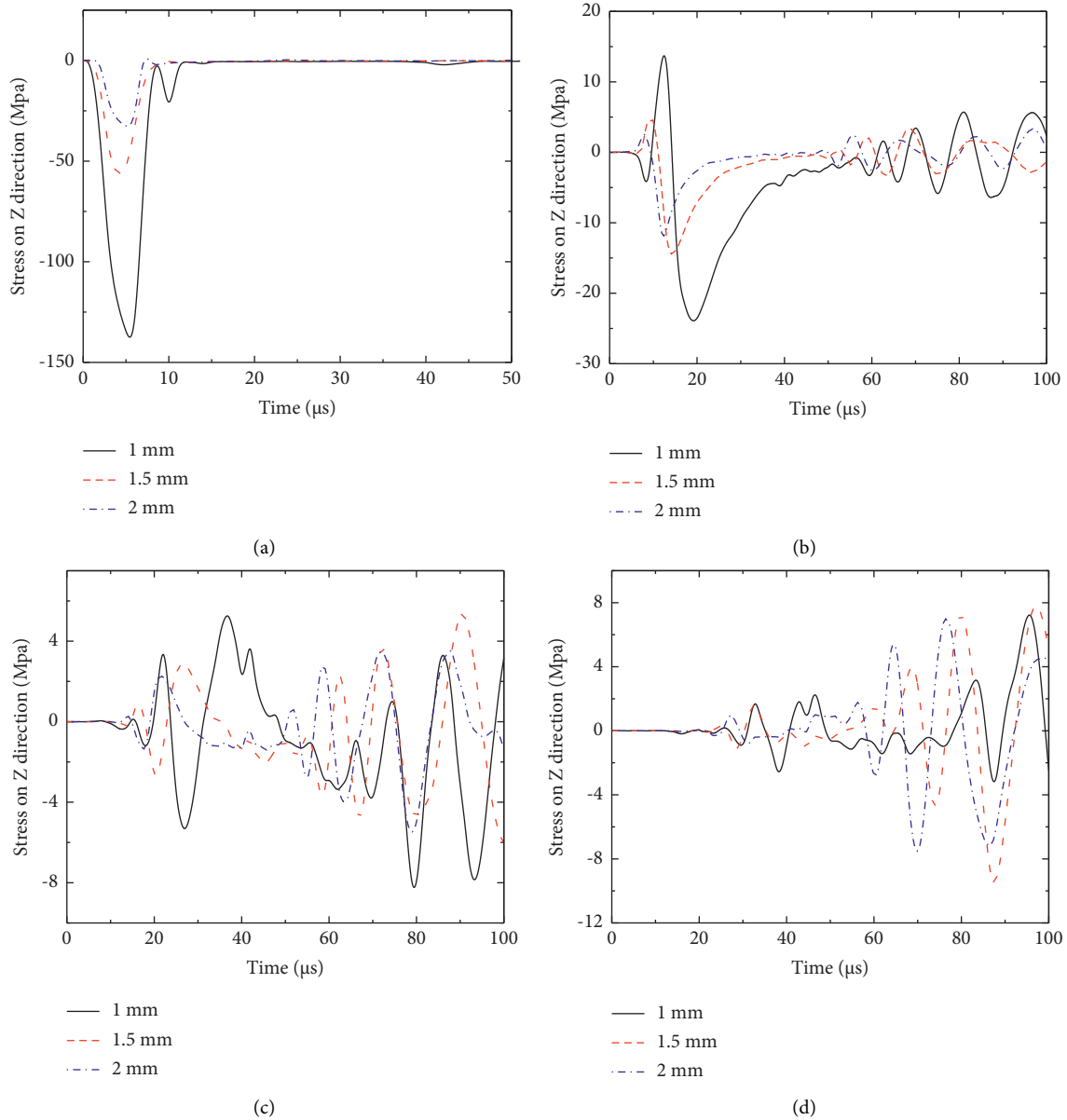
(a)

(b)

(c)

(d)

FIGURE 9: When the impact velocity is 500 m/s, the stress of different thickness steel plates is shown. (a) Point 1; (b) Point 2; (c) Point 3; (d) Point 4.

increases as the thickness of the steel plate increases. When the thickness of the steel plate increases to a critical value, the compression degree will no longer be affected by it, which means that the impact strength suffered remains unchanged [37].

Figures 9 and 10 show the change rule of stress and strain of the steel plate with thickness when the impact velocity of the projectile is 500 m/s. According to the figure, the change rule of stress curve is almost identical to the strain curve. As can be seen from Figure 9(a), at the center point (point 1), the stress-strain value of the steel plate first increases and then decreases when the impact time $t < 15\,\mu$s, remaining is the constant value of zero finally; the peak value decreases as the thickness of the steel plate increases because the projectile collided with the steel plate and recovered its

deformation in the range of $15\,\mu$s. As can be seen from Figures 9(b)–9(d), at 18 mm, 36 mm, and 54 mm from the center point (point 2, point 3, and point 4), the velocity of stress wave propagation and the stress value decrease at point 2 as the thickness of the steel plate increases due to the continuous propagation of stress waves; the stress-strain change values of the projectile with 1.5 mm and 2 mm have little difference at points 3 and 4 because the propagation time increases as the distance to center point increases. At this time, the peak stresses of the steel plate with 1.5 mm and 2 mm are greater than that with 1 mm because the velocity at the tensile wave reflected by the steel plate catches up with the increase in shock wave as the thickness decreases. When the tensile wave exceeds the shock wave, it will be unloaded [38]. Therefore, the thickness has a negligible effect on the
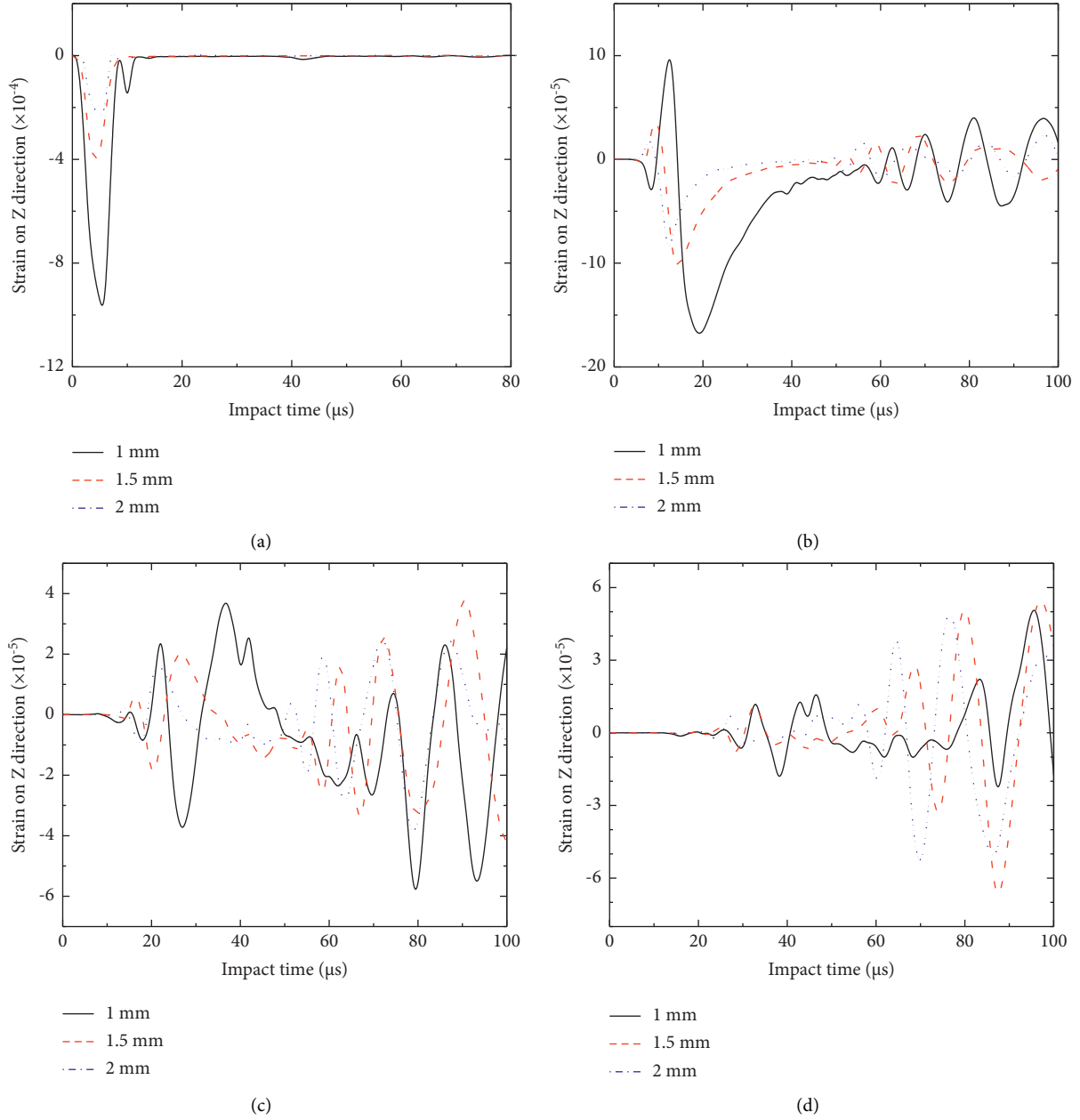
(a)

(b)

(c)

(d)

FIGURE 10: When the impact velocity is 500 m/s, the strain of different thickness steel plates is shown. (a) Point 1; (b) Point 2; (c) Point 3; (d) Point 4.

peak stress-strain of the steel plate, so the equipment cost can be saved.

Drawing on the modified JSC equation based on the Burton Cour-Palais empirical equation of single board cratering proposed by NASA for the "Apollo" plan, it is possible to approximate the impact velocity at the critical penetration of thin plate materials.

The crater depth after the projectile hits the steel plate:

$$h_c = 5.24 D^{19/18} \mathrm{BH}_b^{-0.25} \left(\frac{\rho_p}{\rho_b}\right) \left(\frac{v_n}{C_b}\right)^{2/3}. \tag{5}$$

In the formula, h_c is the pit depth of the steel plate (cm), D is the rod diameter of the projectile (cm), ρ_p is the density of projectile (g/cm^3), ρ_b is the density of steel plate (g/cm^3), BH_b is the Brinell hardness of steel plate (kgf/mm^2), v_n is the normal component of the impact velocity of projectile (km/s), and C_b is the sound velocity of the steel plate material (km/s).

The total energy of the system remains conserved accompanied by dramatic energy changes, so the initial kinetic energy of the projectile is rapidly reduced and transformed into the internal energy and kinetic energy during the impact process. Figures 11(a)–11(c) show the total energy changes of the projectile and the steel plate under different thickness. As can be seen from the figure, the energy of the projectile converts into 1.69 J during the impact process when the thickness of the plate is 1 mm, accounting for 92.5% of the
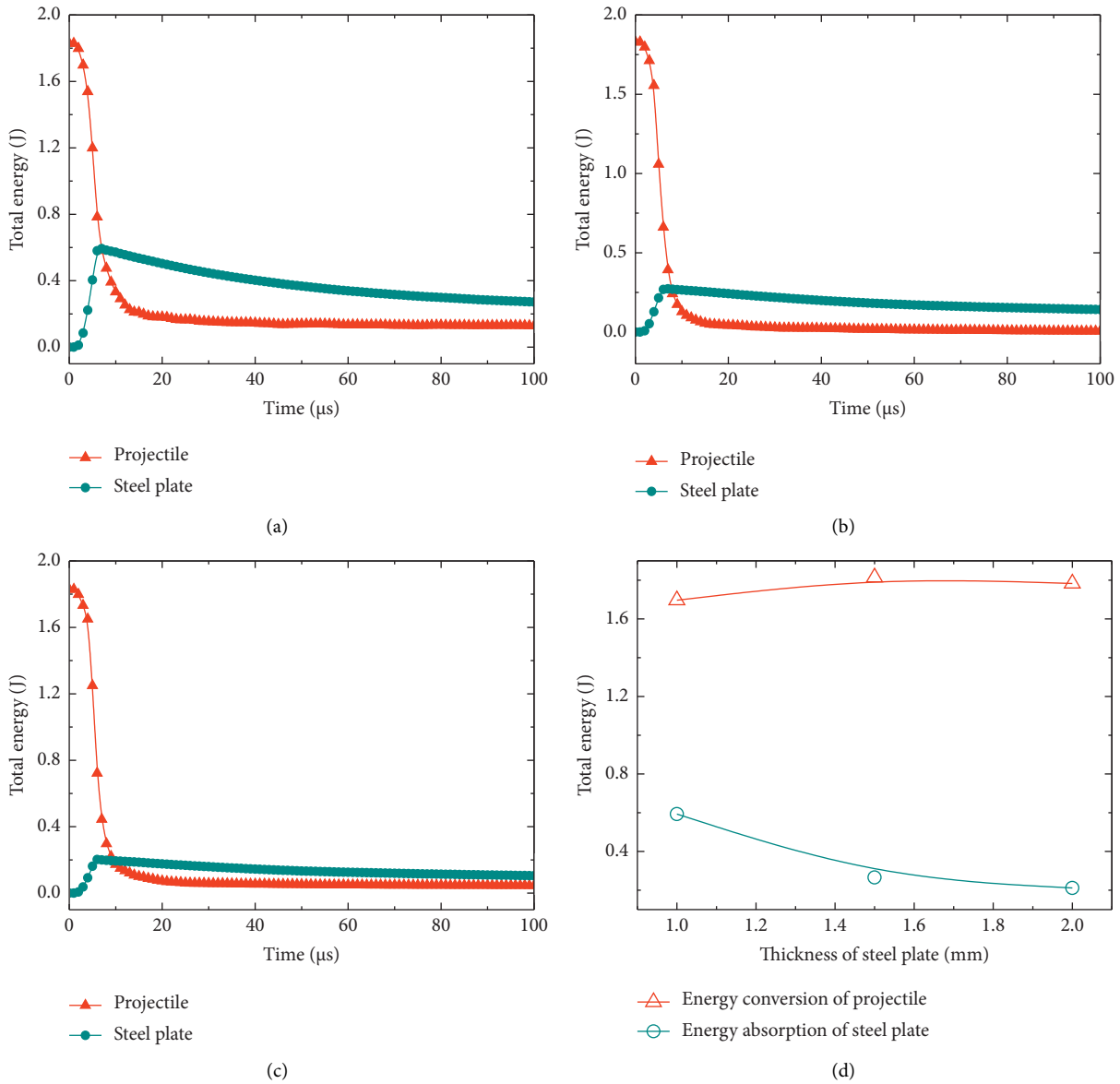
(a)

(b)

(c)

(d)

Figure 11: Figure of the influence of steel plate's thickness on projectile's velocity. (a) Point 1; (b) Point 2; (c) Point 3; (d) Point 4.

initial kinetic energy; the energy of the projectile converts about 1.8 J when the thickness of the steel plate is 1.5 mm and 2 mm, accounting for 99% of the initial kinetic energy, and energy of the projectile eventually tends to zero. The energy absorbed by the steel plate begins to increase, and the projectile is likely to be broken easily as the thickness of the steel plate increases, gradually decreasing and tending to zero. Figure 11(d) shows the relationship between the energy transformed by the projectile and the energy absorbed by the steel plate with the thickness of the steel plate. As can be seen from the figure, the projectile conversion energy of 1 mm steel plate is slightly smaller than that of 1.5 mm and 2 mm steel plates, while the difference of the projectile conversion energy between 1.5 mm and 2 mm steel plates seems to be ignored. It can be concluded that the energy absorbed by the steel plate decreases as its thickness increases. That is to say, the thicker the steel plate is, the more the irreversible

crushing of the pore space makes the energy dissipation less concentrated [39], and the easier the projectile seems to break, the more the energy lost will be.

After the steel plate is hit by the projectile at a high speed, the front surface of the steel plate first deforms to form a crater, while backsplash fragments begin to appear after a period of continuous action of the shock wave. The position where the backsplash starts is farther away from the impact point than that where the projectile begins to break [40–42]. The coal-rock projectile begins to break at the contact point with the steel plate and separates from the main body of the steel plate. However, as the projectile continues to move forward, the upward movement of the contact point of the projectile plate is faster than the upward component of the rebound speed of the steel plate. Finally, the projectile blocks this part of the material from continuing to splash back and makes it follow projectiles move together.

4. Conclusions

(1) The morphological changes of coal-rock projectiles basically include plastic deformation and partial crushing and is completely broken during the entire failure process. However, the steel plate has varied from no obvious deformation to obvious deformation, forming a pit at the impact point, and finally has recovered partial deformation. When the projectile hits the steel plate at high speed, most of its initial kinetic energy continues to be converted into the kinetic energy of the projectile fragments. Meanwhile, the rest of the initial kinetic energy will be used for plastic deformation of the impact body and dynamic crushing.

(2) The duration of the peak stress of the steel plate under the same thickness is affected by the speed and the distance from the center point. The peak stress and its duration on the steel plate increase as the impact speed increases, while the peak stress and its duration decrease as the distance from the center point increases when the impact time $t < 30\,\mu$s. When the impact time $t > 30\,\mu$s, the stress and strain of the steel plate continue to propagate in a trend similar to a sinusoidal curve, and the fluctuation degree of curve and the peak stress vary more obvious as the impact speed increases.

(3) When the impact velocity is 100 m/s and 300 m/s, the deformation caused by the axial velocity presenting arterial changes at the point of impacting the projectile under the same thickness increases as the impact velocity increases. The axial velocity of the projectile increases sharply and then tends to stabilize when the impact velocity reaches over 500 m/s. Based on this, both the energy absorbed by the steel plate and the growth rate of energy increase as the impact velocity increases, while the ratio of the energy absorbed by the steel plate to the initial kinetic energy of the projectile decreases accordingly.

(4) The thickness of the steel plate under the same impact speed has little effect on the damage effect of the steel plate when the thickness of the steel plate is greater than 2 mm. When the thickness of the steel plate is 1.50 mm and 2.00 mm, the size of the fragments differentiates little, which reflects that the fragmentation degree of the main part of the projectile increases first and then does not change with the increase of the thickness of the steel plate. With the increase of the thickness of the steel plate, the irreversible fragmentation of the pore space leads to the decentralization of energy dissipation, and the increase of energy loss makes the probability of projectile fragmentation increase.

Data Availability

The datasets analyzed or used to support the findings of this study are available from the corresponding author on reasonable request.

Conflicts of Interest

The authors declare that they have no conflicts of interest.

Acknowledgments

References

[1] U. Bielert and M. Sichel, "Numerical simulation of premixed combustion processes in closed tubes," *Combustion and Flame*, vol. 114, no. 3-4, pp. 397–419, 1998.

[2] M. Fairweather, G. K. Hargrave, S. S. Ibrahim, and D. G. Walker, "Studies of premixed flame propagation in explosion tubes," *Combustion and Flame*, vol. 116, no. 4, pp. 504–518, 1999.

[3] A. Kravtsov, J. Zdebski, P. Svoboda, and V. Pospichal, "Numerical analysis of explosion to deflagration process due to methane gas explosion in underground structures," in *Proceedings of the International Conference on Military Technologies (ICMT) 2015*, Brno, Czech Republic, May 2015.

[4] J. Xu, C. Zhai, L. Qin, and G. Yu, "Evaluation research of the fracturing capacity of non-explosive expansion material applied to coal-seam roof rock," *International Journal of Rock Mechanics and Mining Sciences*, vol. 94, pp. 103–111, 2017.

[5] Z.-X. Zhang, Y. Qiao, L. Y. Chi, and D.-F. Hou, "Experimental study of rock fragmentation under different stemming conditions in model blasting," *International Journal of Rock Mechanics and Mining Sciences*, vol. 143, Article ID 104797, 2021.

[6] Q. Zhang, B. Qin, H. Yan, and D.-C. Lin, "A methodology to predict shock overpressure decay in a tunnel produced by a premixed methane/air explosion," *Journal of Loss Prevention in the Process Industries*, vol. 44, pp. 275–281, 2016.

[7] C. Zhu, B. Q. Lin, B. Y. Jiang, and Q. Liu, "Numerical simulation on oscillation and shock of gas explosion in a closed end pipe," *Zhendong yu Chongji/Journal of Vibration and Shock*, vol. 31, no. 16, pp. 8–12+17, 2012.

[8] H. Wei, J. Zhao, L. Zhou, Z. Xu, and D. Gao, "Pressure oscillation with destructive effect of flame propagation of a stoichiometric hydrogen-air mixture in a confined space," *Journal of Hazardous Materials*, vol. 344, pp. 1025–1033, 2018.

[9] K. Wang, "Study of the destruction of ventilation systems in coal mines due to gas explosions," *Powder Technology*, vol. 286, pp. 401–411, 2015.

[10] Q. Zhang and Q. J. Ma, "Dynamic pressure induced by a methane–air explosion in a coal mine," *Process Safety and Environmental Protection*, vol. 93, pp. 233–239, 2015.

[11] S. Z. Yang, S. Engineer, and P. Jia, "Study on the Damaging Characteristics of High-Speed Air Flow Produced by Gas Explosion in Coal Mines," *China Safety Science Journal (CSSJ)*, vol. 19, no. 5, pp. 86–90, 2009.

[12] X. Lang, "Study on the Aettenuation Law and Safe Distance of Gas Explosion Shock Wave," *China University of Ming and Technology*, 2015.

[13] A. J. Piekutowski, "Fragmentation-initiation threshold for spheres impacting at hypervelocity," *International Journal of Impact Engineering*, vol. 29, pp. 563–574, 2003.

[14] V. V. Bashurov, G. V. Bebenin, G. V. Belov, Y. N. Bukharev, and G. P. Schlyapnikov, "Experimental modelling and numerical simulation of high- and hypervelocity space debris impact to spacecraft shield protection," *International Journal of Impact Engineering*, vol. 20, no. 1-7, pp. 69–78, 1997.

[15] C. J. Maiden and A. R. Mcmillan, "An investigation of the protection afforded a spacecraft by a thin shield," *Aerospace Sciences Meeting*, vol. 2, no. 11, pp. 1992–1998, 1964.

[16] K. A. Iyer, K. L. Poormon, R. M. Deacon, D. S. Mehoke, and R. C. Brown, "Hypervelocity impact response of Ti-6Al-4 V and commercially pure titanium," *Procedia Engineering*, vol. 58, pp. 127–137, 2013.

[17] J. M. Dahl and P. H. Schultz, "Measurement of stress wave asymmetries in hypervelocity projectile impact experiments," *International Journal of Impact Engineering*, vol. 26, pp. 145–155, 2001.

[18] G. S. Guan, R. T. Niu, and B. J. Pang, "Numerical simulation of al sphere fragmentation under high-velocity normal impacting aluminum mesh bumper," *Gaoya Wuli Xuebao/Chinese Journal of High Pressure Physics*, vol. 27, pp. 671–676, 2013.

[19] S. Yang, "Deformation field in 316L stainless steel by single shot peening," *Explosion and Shock Waves*, vol. 37, pp. 126–133, 2017.

[20] R. Shao, C. Wu, Y. Su, and Z. Liu, "Numerical analysis on impact response of ultra-high strength concrete protected with composite materials against steel ogive-nosed projectile penetration," *Composite Structures*, vol. 220, pp. 861–874, 2019.

[21] T. Wang, H. B. Zhao, Y. Li, H. Zhang, and N. S. Ju, "Simulation and experimental study on the discontinuous dynamic impact on unidirectional confined coal-rock damage," *Shock and Vibration*, vol. 2019, Article ID 9379563, 15 pages, 2019.

[22] Williamsen and Evans, "Predicting orbital debris shape and orientation effects on spacecraft shield ballistic limits based on characteristic length," *International Journal of Impact Engineering*, vol. 33, pp. 862–871, 2006.

[23] Y. I. Rong-cheng and J. R. Yin, "Study on the performance of ceramic composite projectile penetrating into ceramic composite target," *Defence Technology*, vol. 13, p. 5, 2017.

[24] K. Bao, X. Zhang, M. Tan, B. Chen, and H. Wei, "Ballistic Test and Numerical Simulation on Penetration of a boron-carbide-ceramic Composite Target by a Bullet," *Explosion and Shock Waves*, vol. 39, no. 12, pp. 57–68, 2019.

[25] G. Chen, Z. F. Chen, W. F. Xu, Y. M. Chen, and X. C. Huang, "Investigation on the J-C Ductile Fracture Parameters of 45 Steel," *Explosion & Shock Waves*, vol. 27, no. 2, pp. 131–135, 2007.

[26] D. Zhu, B. J. Pang, Y. C. Sun, B. Jia, and Y. P. Cheng, "Damage characteristics resulting from meteoroid high-speed impaction on the spacecraft Whipple shield," *Journal of Astronautics*, vol. 28, no. 1, pp. 94–100, 2010.

[27] M. Lambert, "Hypervelocity impacts and damage laws," *Advances in Space Research*, vol. 19, pp. 369–378, 1997.

[28] L. E. Lamberson, A. J. Rosakis, and V. Eliasson, "In-situ optical investigations of hypervelocity impact induced dynamic fracture," *Experimental Mechanics*, vol. 52, no. 2, pp. 161–170, 2012.

[29] Y. Yang, L. I. Xiaojun, D. Zhu, and W. U. Biao, "Research Development of Materials Damage Effect under Hypervelocity Impact," *Ordnance Material Science and Engineering*, vol. 37, no. 5, pp. 133–140, 2014.

[30] C. C. Gu and M. Q. Shi, "Numerical simulation of high-velocity impact with ANSYS/LS-DYNA," *Xi Tong Fang Zhen Xue Bao/Journal of System Simulation*, vol. 21, pp. 4621–4624, 2009.

[31] L. Sheng-Wei, L. Sen, Q. Jin-Gui, R. Lei-Sheng, and H. Jie, "Comparison of crater behavior of water ice by low and high density projectiles under hypervelocity impact," *Procedia Engineering*, vol. 204, pp. 329–336, 2017.

[32] M. Grujicic, B. Pandurangan, T. He, B. A. Cheeseman, and C. Yen, "Computational investigation of impact energy absorption capability of polyurea coatings via deformation-induced glass transition," *Materials Science and Engineering A*, vol. 527, pp. 7741–7751, 2010.

[33] Z. Han, D. Li, T. Zhou, Q. Zhu, and P. G. Ranjith, "Experimental study of stress wave propagation and energy characteristics across rock specimens containing cemented mortar joint with various thicknesses," *International Journal of Rock Mechanics and Mining Sciences*, vol. 131, Article ID 104352, 2020.

[34] E. Tang, M. Xu, Q. Zhang, and M. Wang, "Study on partitioning of energy in hypervelocity impact on thick target," *Guti Lixue Xuebao/Acta Mechanica Solida Sinica*, vol. 37, pp. 152–160, 2016.

[35] Y. Li, Z. Zhu, B. Li, J. Deng, and H. Xie, "Study on the transmission and reflection of stress waves across joints," *International Journal of Rock Mechanics and Mining Sciences*, vol. 48, pp. 364–371, 2011.

[36] J. Zhang, Z. Liu, S. Fu, and G. Qiao, "Damage of rock mass by double-hole blasting with slit charge and development of stress wave under high in situ stress," *Shock and Vibration*, vol. 2022, Article ID 6967057, 11 pages, 2022.

[37] Z. Jia, C. Li, R. Zhang, M. Wang, and J. Xie, "Energy evolution of coal at different depths under unloading conditions," *Rock Mechanics and Rock Engineering*, vol. 52, pp. 4637–4649, 2019.

[38] R. Chi, "Experimental investigation for deformation and fragmentation of spheres penetrating sheets at hypervelocity," *Baozha Yu Chongji/Explosion and Shock Waves*, vol. 29, pp. 231–236, 2009.

[39] T. Hoerth, F. Schafer, J. Hupfer, O. Millon, and M. Wickert, "Momentum transfer in hypervelocity impact experiments on rock targets," *Procedia Engineering*, vol. 103, pp. 197–204, 2015.

[40] Y. Yang, Q. Zeng, and L. Wan, "Dynamic response analysis of the vertical elastic impact of the spherical rock on the metal plate," *International Journal of Solids and Structures*, vol. 158, pp. 287–302, 2019.

[41] Y. Yang and Q. Zeng, "Influence Analysis of the Elastic Supporting to the Dynamic Response when the Spherical Rock Elastic Impacting the Metal Plate and to the Coal Gangue Impact Differences," *IEEE Access*, vol. 7, p. 1, 2019.

[42] C. Liu, X. Zhang, H. Chen, J. Wang, and W. Xiong, "Experimental and theoretical study on steel long-rod projectile penetration into concrete targets with elevated impact velocities," *International Journal of Impact Engineering*, vol. 138, Article ID 103482, 2019.